Acta Materialia 276 (2024) 120123

Contents lists available at ScienceDirect

Acta Materialia

journal homepage: www.elsevier.com/locate/actamat

Full length article

Partial melting nature of phase-change memory Ge-Sb-Te superlattice uncovered by large-scale machine learning interatomic potential molecular dynamics

Bai-Qian Wang [a], Tian-Yu Zhao [a], Huan-Ran Ding [a], Yu-Ting Liu [a], Nian-Ke Chen [a,*], Meng Niu [a], Xiao-Dong Li [a], Ming Xu [b], Hong-Bo Sun [c], Shengbai Zhang [d], Xian-Bin Li [a,*]

[a] State Key Laboratory of Integrated Optoelectronics, College of Electronic Science and Engineering, Jilin University, 130012 Changchun, China
[b] School of Integrated Circuits, Huazhong University of Science and Technology, 430074 Wuhan, China
[c] State Key Lab of Precision Measurement Technology and Instruments, Department of Precision Instrument, Tsinghua University, 100084 Beijing, China
[d] Department of Physics, Applied Physics, and Astronomy, Rensselaer Polytechnic Institute, 12180 Troy, New York, United States

ARTICLE INFO

Keywords:
Phase-change memory
Ge-Sb-Te superlattice
Partial melting
Molecular dynamics
Machine learning interatomic potential

ABSTRACT

$[GeTe]_m$-$[Sb_2Te_3]_n$ superlattice (GST-SL) is a promising material candidate to solve the critical problem of high-power consumption for phase-change memory technology. However, the switching mechanism is still under strong debate during the last decade. A key controversial question is that whether melting in GST-SL is possible. In this work, a large-scale machine learning interatomic potential (MLIP) molecular dynamics (MD) simulation with a one-order-of-magnitude larger atom number than that of conventional density functional theory (DFT) MD captures a unique partial melting behavior in GST-SL, where a *sparse-nucleation-and-growth* governed melting behavior is triggered by the flipping of atoms into van der Waals (vdW) gaps and forming cation-in-vdW-gap (CiV) defect as starting point, and then is slowly developed via propagating liquid-crystalline interfaces. In great contrast, the traditional melting of rock salt (RS)-GST occurs very fast due to instant homogeneous nucleation from high-density intrinsic vacancies distributed randomly in its cubic lattice. Therefore, the melting regions in GST-SL can be spatially localized in form of partial melting and are readily controlled. Moreover, the atomic distribution after melting in GST-SL is more chemical ordering than that in RS-GST. By the large-scale MLIP-MD, the present study provides a critical atomic insight into GST-SL phase-change behaviors that conventional DFT-MDs hardly achieve. This partial-melting nature in GST-SL helps explain the long-term-confused working principle of GST-SL-based phase-change memory, which will accelerate its application in the big-data era.

1. Introduction

Phase-change memory (PCM) technology is considered a promising candidate for storage-class memory (SCM) [1,2] because it has a faster recording speed compared to conventional non-volatile memory (NVM) technologies such as hard disk drive (HDD) and flash memory. Moreover, in recent years, PCM has attracted widespread attention owing to its excellent prospects in neuromorphic computing [3,4], in-memory computing [5-7], flexible display [8,9], all-optical NVM [10], tunable meta-surface [11] and photonic-electronic hybrid computing [12,13]. However, despite these advantages, the application of PCM still suffers from the high-power consumption problem due to its large energy cost of phase transitions [14]. To overcome the problem of power consumption, many efforts have been made including miniaturization of devices or electrodes [15], suppression of thermal dissipation [16,17], and development of new materials [18-21]. Among them, the $[GeTe]_m$-$[Sb_2Te_3]_n$ superlattice (GST-SL) has attracted intensive attention for more than 10 years owing to its potentially novel mechanisms [22-25]. However, though many mechanisms have been proposed, they are still under strong debate up to now [26-30].

These previous mechanisms can be approximately classified into two types: (1) order-to-order phase transitions without melting via Ge-atom flipping or stacking-fault movements [31-34]; (2) Partial melting/amorphization of the regions near the electrodes or van der Waals (vdW)

* Corresponding authors.
E-mail addresses: chennianke@jlu.edu.cn (N.-K. Chen), lixianbin@jlu.edu.cn (X.-B. Li).

https://doi.org/10.1016/j.actamat.2024.120123
Received 19 February 2024; Received in revised form 17 June 2024; Accepted 19 June 2024
Available online 20 June 2024

interfaces [35-37]. For the first-type mechanisms, there still are several problems in previously proposed models. For example, the energy barriers of the whole atomic layer flipping are high [34]. Also, the signal contrast between the two crystalline phases is not large enough [33]. Moreover, these models rely on specific atomic structures of GST-SL, such as the Ferro/Petrov/inverted-Petrov models or the stacking faults [29,30,38]. However, many experiments have demonstrated that low power consumption is a general advantage in superlattice and superlattice-like materials with different compositions [36,39,40]. In addition, the low-power consumption behavior does not rely on a directional electric field as it still works under laser irradiations [22]. In brief, a more general mechanism that can apply to different superlattice materials and their electronic/optical devices is urgently required.

For the second-type mechanisms, melting/amorphization in GST-SL is feasible. Such an opinion has also been reported and discussed in previous articles [38,41,42]. Recently, in a GST-SL PCM device, a much smaller amorphized area rather than the thick mushroom-shaped amorphous region in rock salt (RS)-GST near the electrode is observed by high-resolution STEM [37]. The reason for the formation of the smaller amorphous region and the improved performances of GST-SL is attributed to the thermal or electrothermal confinement effect [37,42]. Corresponding finite element electro-thermal simulations show the anisotropic electrical/thermal conductivities and the large thermal boundary resistance between GST-SL and electrodes, which may lead to a more localized melting/amorphization area compared to the case of conventional PCM devices [37,43]. However, the mechanism is still doubted due to the lack of dynamic and atomic studies for the GST-SL melting behavior. *Ab initio* molecular dynamics (AIMD) simulation has been demonstrated to be a proper approach to investigate homogeneous melting processes in conventional RS-GeSbTe [30,35]. However, the simulation scale of AIMD is limited to only several hundred of atoms, which is far from enough to describe anisotropic atomic motion like the case in GST-SL with multiple interfaces.

Using machine learning interatomic potentials (MLIP) from DFT datasets for MD simulations has emerged as a very promising method to substantially extend the MD-simulation scale with the quantum-mechanics precision [44-47]. For example, large-scale MD simulations based on the neural network potential [45] or Gaussian Approximation Potential (GAP) [44] have revealed various important phenomena in PCM materials including the breakdown of the Stokes–Einstein relation in supercooled liquid of GeTe [48], the dynamical heterogeneity in supercooled liquid of GeTe [49], the interface effect in the crystallization of GeTe [50], the origin of the first sharp diffraction peak in amorphous GST [51], the origin of gap states in amorphous GST [52], the finite-size effect of crystallization in GST [53] and so on [54,55]. Furthermore, device-scale simulations of PCM using GAP were recently reported [56]. Therefore, the MLIP-MD will bring a new opportunity to clarify the critical phase-transition mechanism for the system of GST superlattice.

In this work, we investigate atomic dynamics of melting behavior in GST-SL for the first time by a large-scale MLIP-MD (with >3000 atoms), using the GAP developed by Elliot et al. [51]. The training set of the Ge-Sb-Te machine learning potential consists of elemental, binary, ternary crystals, liquid, and amorphous samples of these three elements, so the machine learning interatomic potential can well describe the melting and quenching process of GST and is applied in related works [51,57]. The present MD simulations reveal an unexpected "*sparse-nucleation-and-growth*" governed melting behavior in GST-SL. In great contrast, the melting of conventional cubic RS-GST is "*ultra--dense-nucleation*" dominated. As a result, partial or local melting of the GST-SL is readily achieved whereas the melting of the RS-GST is in a form of a global way and difficult to be controlled. This signifciant difference is attributed to huge discrepancy in their structures, i.e. the stable vdW interfaces in GST-SL vs. the randomly distributed vacancies in RS-GST. This work uncovers the nature of partial melting of GST-SL from the point of view of atomic dynamics, which will provide insightful understanding and critical reference for the optimization/design of GST superlattice-based PCM technology in the big-data era.

2. Methods of computation and analysis

The molecular dynamics process was simulated by LAMMPS software [58]. Interatomic interactions are provided by GAP potential developed for GST materials [51]. Structures were relaxed until reaching the stopping tolerance 1×10^{-12} for energy (unitless) before molecular dynamics simulations. Although the GAP potential does not include vdW corrections, the width of the vdW gap in the Kooi GST-SL model [28] is 2.60 Å while the one calculated from DFT+D3 is 2.80 Å. The results are still close. The canonical ensemble (NVT) is applied to the molecular dynamics simulation with a time step of 3 fs, the temperature was controlled by a Nose-Hoover thermostat, and structures are kept at a temperature of 300 K for a period of time to get their thermal equilibrium states at room temperature before heating/melting.

The smooth overlap of atomic positions (SOAP) similarity kernel can quantify the similarity between two atomic environments [59]. An environment of a certain atom within r_c, reflecting by atomic density distribution $\rho(r)$ centered around the atom, can be represented by a sum of Gaussian functions with broadness σ on each neighbor atomic position, and the atomic density is then expanded on a basis of radial functions $R_n(r)$ and spherical harmonics $Y_{lm}(r)$ as,

$$\rho(r) = \sum_i \exp\left(-\alpha|\boldsymbol{r}-\boldsymbol{r}_i|^2\right) = \sum_{nlm} c_{nlm} R_n(r) Y_{lm}(\hat{\boldsymbol{r}})$$

the power spectrum $p(\xi)$ of atomic environment ξ is transferred into a unit-length vector $\hat{\boldsymbol{p}}(\xi)$ [60], and the similarity of two atomic environment can be calculated as,

$$k(\xi,\xi') = \hat{\boldsymbol{p}}(\xi)\cdot\hat{\boldsymbol{p}}(\xi')$$

The larger the value of $k(\xi,\xi') \in [0,1]$, the more similar atomic environments are. Based on the atomic environments in the crystalline phase, the atoms can be classified into three species [Ge/Sb (O:6), Te (TY:3), Te (O:6)] in GST-SL and two species [Ge/Sb (cation), Te (anion)] in RS-GST. The similarity of an atom to its crystalline phase environment is the average of the similarities of the atom to each atom of the same species in the reference (crystalline) structures, which are randomly chosen in their 300-K MDs, see Fig. S1 in Supplementary Material. For Te atoms in GST-SL, due to the existence of the vdW gap, the Te atoms in trigonal non-coplanar coordination (TY:3) near the vdW gap and those in octahedral coordination (O:6) inside the layer block are classified into two Te species. When judging whether an atom is in a crystalline or liquid/disordered phase, we compare its local atomic environment through the SOAP similarity kernel. According to our test, the crystalline and liquid phases can be well distinguished with the threshold values of $k(\xi,\xi')$ for GST-SL (0.85) and RS-GST (0.91), see Fig. S3 in Supplementary Material.

The deviation of bond angle distribution (D_{BAD}) is applied to quantify the local structure and the degree of lattice disorder. The D_{BAD} is calculated as,

$$D_{BAD} = \sqrt{\frac{\sum_i (\theta_i - 90^\circ)^2 + \sum_j (\theta_j - 180^\circ)^2}{i+j}}$$

Where θ is the bond angles. Note that the bond angles are divided into two ranges, $0^\circ \le \theta_i \le 135^\circ$ *and* $135^\circ < \theta_j \le 180^\circ$, to evaluate the structural deviation from the crystalline octahedral configuration where the bond angles are $\sim 90^\circ$ and $\sim 180^\circ$. As such, the larger the D_{BAD} value, the higher the degree of disorder. Here, the *atomic* D_{BAD} is calculated from the bond angles of a single atom, thus measuring the distortion degree of the local environment of the individual atom. On the other hand, the *global* D_{BAD} is calculated from all bond angles within a

structure to quantify the overall distortion degree of the whole structure.

To estimate the spatial localization of melting regions, a localization-degree indicator (LDI) is employed resembling the electronic inverse participation ratio (IPR) [61]. Firstly, the structural model is divided into N blocks of equal size. Secondly, the D_{BAD} is calculated for all bond angles in each block. Then, the LDI is calculated as,

$$LDI = N^6 \times \frac{\sum_i D_{BAD}^6(i)}{\left[\sum_i D_{BAD}(i)\right]^6}$$

where $N = 128$ here and $D_{BAD}(i)$ is the D_{BAD} of the i^{th} block. A higher LDI suggests that the spatial distribution of disordered regions is localized (like the case of partial melting) while a smaller LDI means the distribution is homogenous.

3. Results and discussion

To compare the melting behaviors of GST-SL and RS-GST, we perform high-temperature MD simulations for both systems using large supercells. Here, the model of GST-SL contains 3024 atoms and that of RS-GST has 3112 atoms, which is ten times larger than those of typical AIMDs (100 ~ 300 atoms) [19,62]. The GST-SL model is composed of $Ge_2Sb_2Te_5$, Sb_2Te_3, and $Ge_1Sb_2Te_4$ layer blocks according to the experimental observation [28].

After heating GST-SL to 1100 K and RS-GST to 1000 K, both structures melt but the time required varies greatly. The time evolution of pair correlation function (PCF) and bond angle distribution (BAD) in respective Figs. 1(a) and (b) quantitatively demonstrate that the structure loses its long-range order upon melting in GST-SL. Fig. 2(a) shows the initial structure of GST-SL, and Figs. 2(b)-(e) show several critical snapshots during its melting process. It is found that the melting behavior always begins from a thermally activated point defect, i.e., the flipping of an atom from a layer block into its adjacent vdW gap and leaving a vacancy in the lattice. For instance, at 7.6 ps [Fig. 2(b)], an Sb atom [highlighted by a red ellipse] has flipped into a vdW gap and then the lattice around the defect starts to have a certain degree of distortion at 21.6 ps [see Fig. 2(c)]. Subsequently, melting occurs around the center of the cation-in-vdW-gap (CiV) defect (here, the cations are Ge and Sb, and the anions are Te). Similar processes occur at different times, such as 39.9 ps and 51.0 ps [see Figs. 2(d)-(e)]. It is concluded that the CiV defect in GST-SL can act as a liquid nucleus of its melting.

The PCF and BAD in Figs. 1(c) and (d) show the melting in traditional RS-GST. Firstly, the melting speed of RS-GST is sufficiently faster than that of GST-SL. As shown in Fig. 2, in the present models, starting from 1100 K (note that the typical melting point of GST is ~ 900 K [63]), the melting of GST-SL takes several tens of picoseconds while RS-GST loses its long-range order within just several picoseconds at 1000 K, at least half an order of magnitude faster. The underlying reason for the different melting speeds between GST-SL and RS-GST is due to the different ways of melting nucleation. For GST-SL, the crystalline area can be easily overheated until the CiV defects occur, which needs incubation and propagation times. However, all parts of the RS-GST model simultaneously turn into disordered phases shortly due to the pre-existence of random distributed high-density intrinsic vacancies, which act as natural seeds of nuclei for its ultrafast melting [Figs. 2 (f)-(j)].

Since the CiV defect play a critical role in melting of GST-SL, it is necessary to understand the microscopic formation process of the defect. After carefully observing the movement of atoms in the black square of

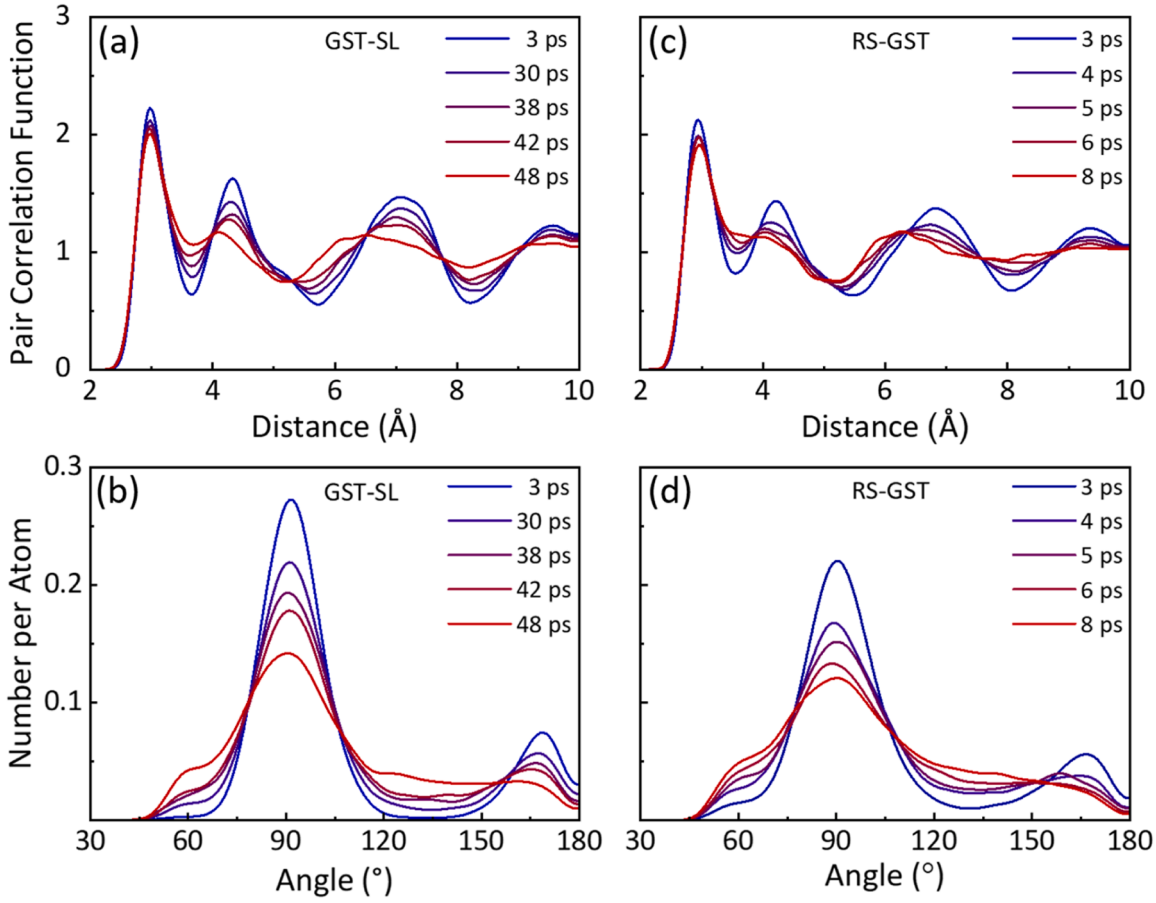

Fig. 1. The time evolutions of (a) the pair correlation function (PCF) and (b) the bond angle distribution (BAD) for GST-SL during the melting process at 1100 K. (c) The time evolution of PCF and (d) BAD for RS-GST during the melting process at 1000 K. Note that the time for GST-SL is significantly longer than that for RS-GST.

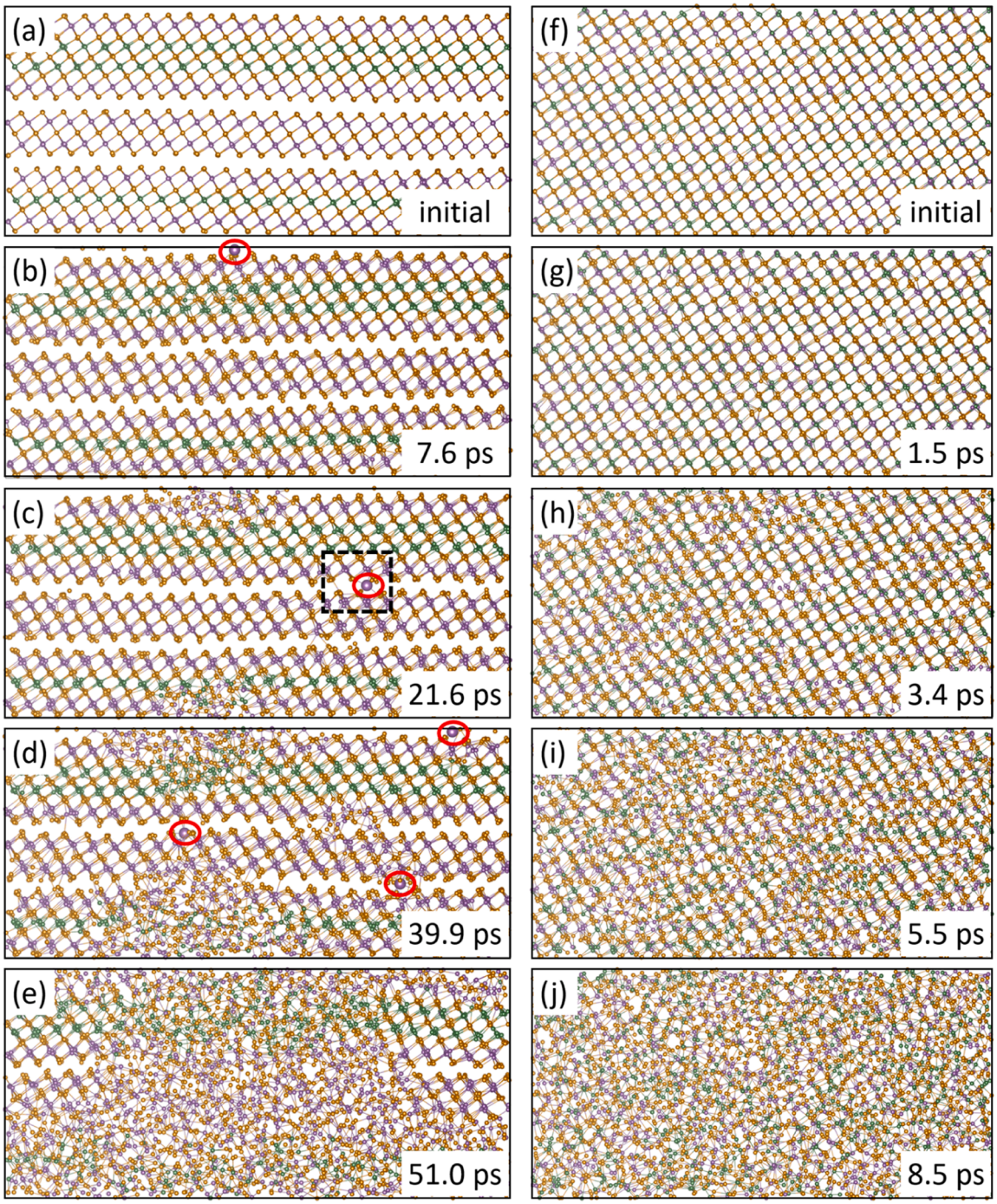

Fig. 2. Snapshots of atomic structures of (a)-(e) GST-SL at 1100 K and (f)-(j) RS-GST at 1000 K during the large-scale MDs of thermal melting. The highlighted atoms in the red ellipses indicate the atoms that flipped into the vdW gaps during the melting process. The black dash-line square in (c) highlights the region that will be used for further studying the formation of cation-in-vdW-gap (CiV) defect later in Fig. 3. Here, the green, purple, and orange balls represent the Ge, Sb, and Te atoms, respectively.

Fig. 2(c), we find that, instead of the direct flipping of Sb atoms into the vdW gap, the anti-site defect of Sb_{Te} near the vdW gap is formed before the formation of CiV. The formation of anti-site defects requires a collective movement of several atoms, as shown in Fig. 3. Fig. 3(a) shows the direction of chain-like movement of Te-Sb-Te-Sb at high temperatures. This movement will form interstitial Sb (Sb_i), leave vacancies (V_{Sb}, V_{Te}) in the original lattices, and form the anti-site defect Te_{Sb} as shown in Fig. 3(b). Then, the vacancies are filled in a cross-exchange manner to form an anti-site defect (Sb_{Te}) near the vdW gap [see Fig. 3(c)]. This anti-site Sb atom then enter the adjacent vdW gap and eventually form a CiV defect [Fig. 3(d)].

According to the DFT based nudged elastic band (NEB) method and a simplified Kooi GST-SL model, we also evaluate the energy barriers of forming the anti-site defect (2.72 eV) and the CiV defect (2.37 eV), see Fig. S2 in Supplementary Material. Although, these values are close to the activation energy (2.56–3.10 eV) per Ge atom in the previous flipping mechanism [64], the working principles are quite different. In our proposed melting mechanism, even a single CiV defect can trigger the nucleation and growth of melting area around the defect in GST-SL. In contrast, in the flipping mechanism, all the atoms in the whole Ge layer

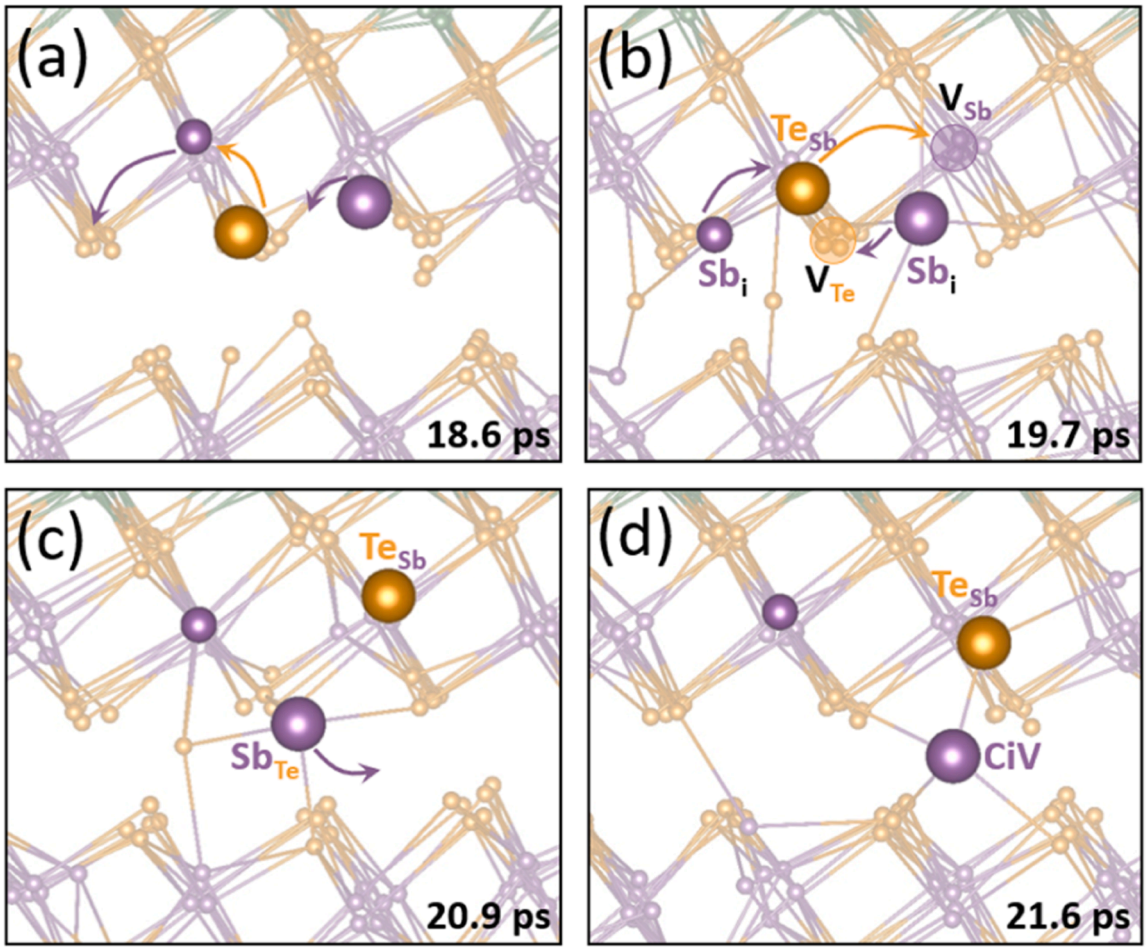

Fig. 3. Snapshots of atomic structures in turn during the formation process of the cation-in-vdW-gap (CiV) defect in GST-SL. (a) Direction of the initial chain-like movement of Te-Sb-Te-Sb that will produce interstitial atoms (Sb_i) and vacancies (V_{Sb}, V_{Te}) in (b). (b) Formation path of Sb-Te anti-site defect by vacancy-assisted site exchange. (c) The formed anti-site defect and its instability. (d) Sb atom enters the vdW gap and forms a CiV defect. The arrows indicate the directions of the atomic movements. The large balls highlight the key atoms of these processes.

are required to flip together, indicating it may be more difficult to happen. Indeed, the flipping mechanism cannot be observed in the present large-scale MLIP MD.

To sum up, the formation of CiV defects need to undergo a series of critical steps and overcome their barriers. As such, the number of CiV defects in GST-SL is far less than the number of intrinsic vacancies in RS-GST. In other words, the nucleation sites for the melting of GST-SL are relatively sparse compared to the ultra-dense nucleation sites in RS-GST.

To quantitatively catch the time evolution of melting regions, a quantitative identification of the melting/disordered area is needed. Here, we use the similarity kernel based on the SOAP [59] to distinguish the liquid and crystalline regions by quantifying the similarity between a specific atom and the atoms in the crystalline phase (see Methods section for more details). The SOAP has been used as a descriptor by machine learning models for fitting interatomic potentials and can also be used to analyze the structural similarity of atoms in different phases [65–67]. Here, we judge whether an atom is in a crystalline state during phase transition by comparing its local atomic environment with those of atoms in a reference crystalline phase. According to our test, the threshold values of similarity $k(\xi, \xi')$ to distinguish the crystalline and liquid phases are chosen as 0.85 for GST-SL and 0.91 for RS-GST, see Fig. S3 in Supplementary Material. Therefore, we choose the color-coding SOAP similarity ranges of 0.8–0.9 for GST-SL and 0.85–0.95 for RS-GST to highlight the phase evolution during the melting, see Fig. 4. As such, the red atomic areas indicate the disordered liquid region while the blue areas are for the crystalline region. The approximate boundaries of the disordered regions in GST-SL are marked with pink lines in Figs. 4(a)-(b). The results suggest that the melting of GST-SL happens in a way of the propagation of disordered regions [Figs. 4(a)-(b)]. When part of the material becomes disordered by the CiV-induced melting, the surrounding crystalline regions remain relatively stable. Then, the disordered area continuously enlarges or grows with time. In contrast, the melting of RS-GST homogeneously takes place from anywhere throughout the entire lattice [Figs. 4(c)-(d)].

The underlying origin can be attributed to the different orders of vacancy distribution in GST-SL and RS-GST. For GST-SL, the vacancies are orderly arranged to form the stable vdW interfaces. Then, each layer block in GST-SL can be independently stabilized owing to the vdW interactions. Therefore, this stability in GST-SL layer blocks can be maintained until the vdW interface is disturbed by the CiV defects. Once a small disordered region appears, it will destroy the adjacent vdW interface, thereby destabilizing the surrounding lattice. In this way, the disordered region grows larger and larger by expanding the order-disorder interfaces. We conclude it as a *sparse-nucleation-and-growth* process. In contrast, intrinsic vacancies in RS-GST are evenly separated and provide spaces for atom vibration and diffusion, thereby acting as seeds of nucleation. The nucleation sites are so dense that the initial liquid nuclei are directly connected without obvious propagations or growth. Correspondingly, we call it an *ultra-dense-nucleation* process. As a result, GST-SL can be partially melted under a homogenous thermal bathing condition, whereas RS-GST cannot. Note that the way of the propagation of melting areas, i.e., *sparse-nucleation-and-growth*, in GST-

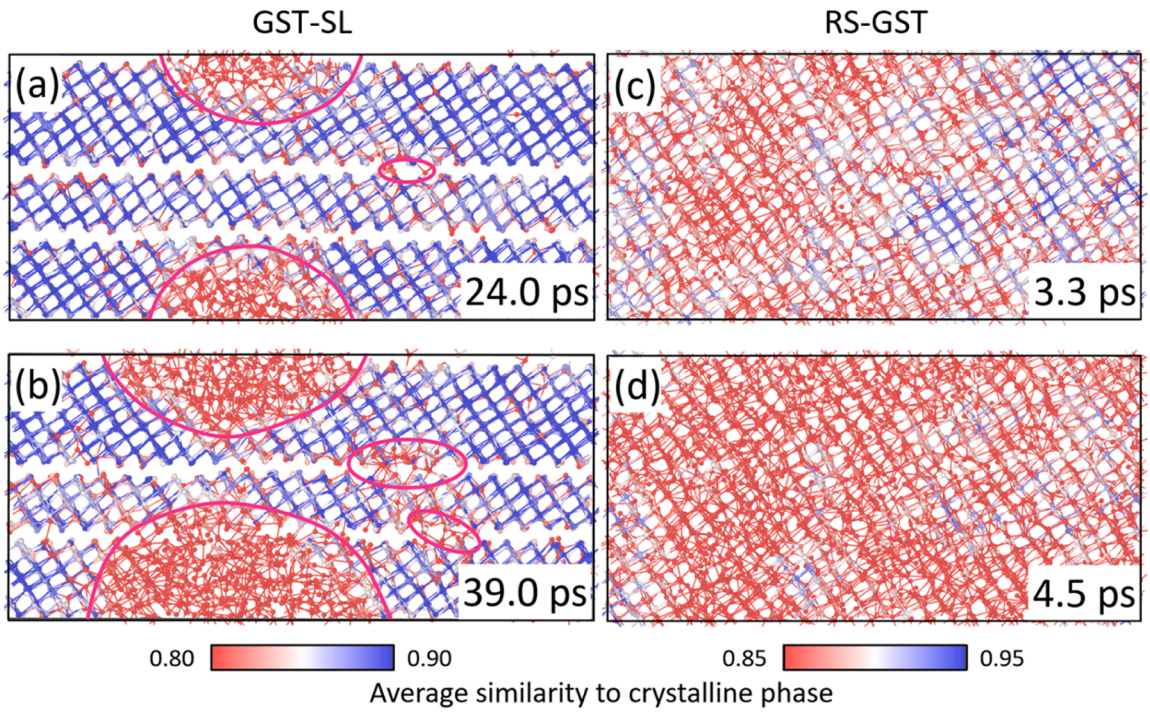

Fig. 4. Characterization of the melting process based on the SOAP similarity kernel. Snapshots of atomic structures of (a)-(b) GST-SL and (c)-(d) RS-GST during their melting processes. The color coding indicates the similarity to the crystalline phase to identify the melting processes. The red and blue colors indicate the liquid region and crystalline region, respectively. The approximate boundaries of the disordered regions in GST-SL are marked with pink lines in (a)-(b).

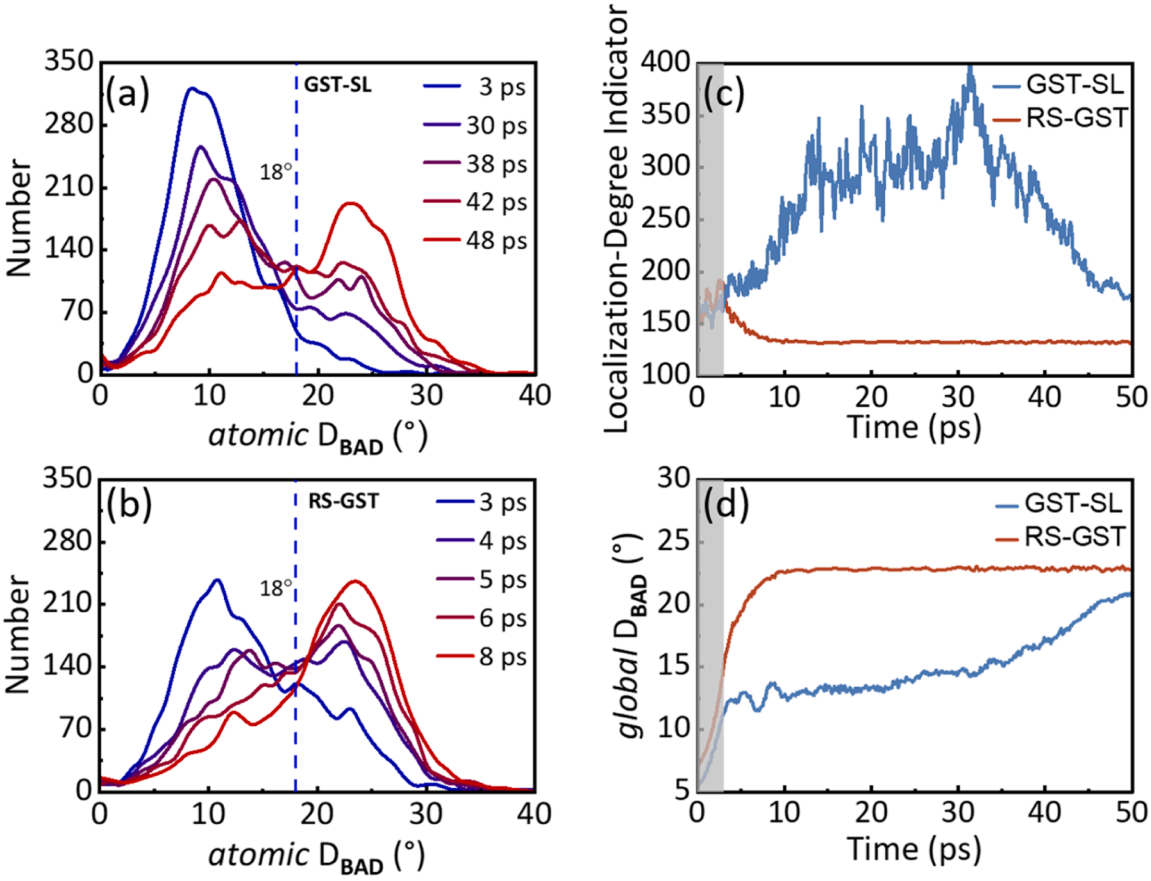

Fig. 5. Atomic-scale characterization of the melting process by deviation of bond angle distribution, D_{BAD}. The time evolutions of the distribution of the *atomic* D_{BAD} during the melting of (a) GST-SL and (b) RS-GST. The time evolutions of (c) Localization-degree indicator (LDI) and (d) the *global* D_{BAD} during the melting of GST-SL and RS-GST. The shaded regions in Figs. 5(c) and (d) indicate the heating-up stage from 300 K, to 1100 K for GST-SL and 1000 K for RS-GST, respectively.

SL is also a reason for its relatively slow melting speed. Both the slow melting speed and the propagation manner suggest that the melting of GST-SL is more readily controlled compared to the case of RS-GST.

Next, to trace the change in local atomic structures during the melting, we further employ an indicator named deviation of bond angle distribution (D_{BAD}) [18] which can reflect the difference between liquid and crystalline phases. Here, the D_{BAD} measures how much the bond angles deviate from 90° or 180°. For crystalline GST-SL and RS-GST, the bond angles around an atom are closed to 90° and 180° due to the standard *p*-orbital bonding characteristic [18]. When they are melted, most of the bond angles will deviate from 90° and 180°. Therefore, the D_{BAD} for bond angles of an individual atom (*atomic* D_{BAD}) can also reasonably estimate the degree of disorder of its local environment.

Figs. 5(a) and (b) show the time evolutions of the distribution of *atomic* D_{BAD} of GST-SL and RS-GST, respectively. Before melting, the *atomic* D_{BAD} is mainly located around 10° due to thermal fluctuations. Then, the *atomic* D_{BAD} gradually increases with melting. After melting, the main peak of *atomic* D_{BAD} is located around 23°. Interestingly, we found that the *atomic* D_{BAD} of 18° is just the watershed between crystalline and liquid phases. Therefore, we use this value to approximately distinguish the crystalline and liquid phases. Figs. S4 and S5 depict the evolution of liquid regions based on this criterion. It can be directly observed that the liquid regions in GST-SL are spatially localized, while the liquid regions in RS-GST are uniformly distributed.

To quantitatively characterize the localization of the melting regions, we introduce a localization-degree indicator (LDI, more details can be found in Methods section), resembling the inverse participation ratio (IPR) [61] which has been used to estimate the localization of electronic states. Similarly, a large value of LDI means the distribution of the melting regions is localized while a small LDI indicates a delocalized melting or no melting. Fig. 5(c) shows the time evolutions of the LDI of GST-SL and RS-GST. To fairly compare the LDIs of GST-SL and RS-GST, the *global* D_{BAD} (calculated from all bond angles in the structure), reflecting the overall degree of melting, are also presented in Fig. 5(d). For RS-GST, the LDI remains small during the melting process and the rapid increase of the *global* D_{BAD} shows the melting is completed within

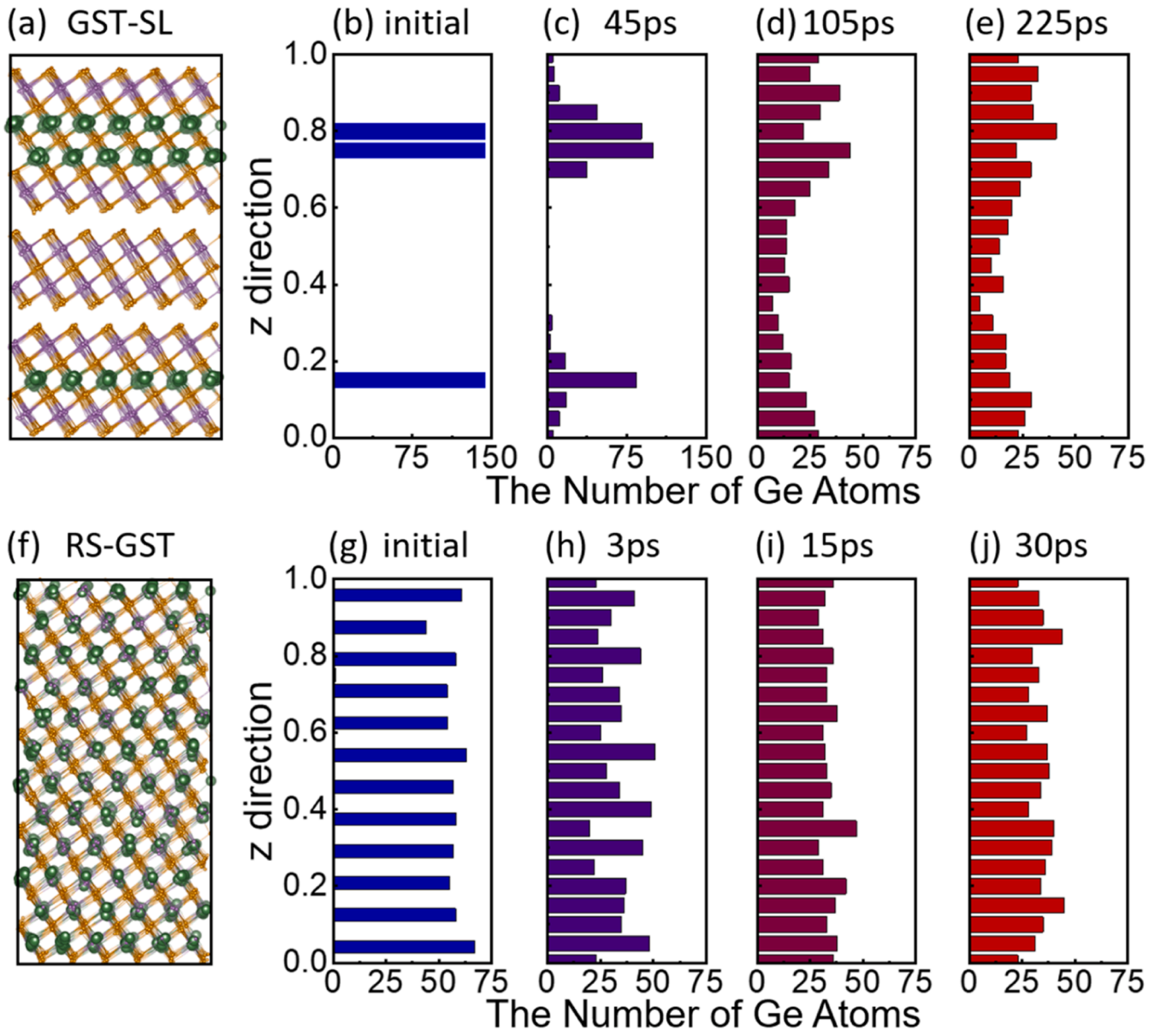

Fig. 6. Evolution of Ge atomic distribution with time during the melting processes of GST-SL and RS-GST. (a) The initial structure of GST-SL. (b)-(e) Distribution of Ge atoms at different times starting from the GST-SL structure. (f) The initial structure of RS-GST. (g)-(j) Distribution of Ge atoms at different times starting from the RS-GST structure. The Ge atoms are highlighted by the green balls in (a) and (f).

10 ps in the present model. For GST-SL, the LDI gradually increases to much higher values with the melting, which unambiguously demonstrates the localized behavior of the melting. Additionally, unlike RS-GST, the increase of *global* D_{BAD} for GST-SL is relatively slow, which is consistent with previously observed lower melting rates due to the melting form of *sparse-nucleation-and-growth*. Therefore, the partial melting behavior of GST-SL is mostly possible. The accompanying video 1 and video 2 capture both of these melting processes.

The localized melting behavior of GST-SL can also result in different liquid structures, at least near the crystalline-liquid interface. For example, in the GST-SL model shown in Fig. 6(a), the initial distribution of Ge atoms naturally gathers at specific layers due to the existence of Sb_2Te_3 layer blocks [28], see Fig. 6(b). The localized melting behavior of GST-SL prevents Ge atoms from fully diffusing within 105 ps as Figs. 6(c) and (d) show. Even after the GST-SL is heated at 1100 K for more than 200 ps [Fig. 6(e)], the Ge atoms distribution still retains a trace of the initial distribution, indicating a certain degree of chemical order (as the crystalline GST-SL has) even after a relatively long melting time. However, in RS-GST, there is no isolated distribution of Ge atoms along the z-direction at the initial structure [Figs. 6(f) and (g)]. During the melting process, the Ge atoms are always homogeneously distributed, as shown in Figs. 6(h)-(j), indicating a full chemical disorder in a diffusive liquid state. The difference in the distribution of atoms in the two melting processes may also be inherited in their amorphous regions by quenching their melting states, which guarantees the element distribution and chemical ordering in GST-SL is less disturbed between its SET state and RESET state. What's more, the chemical order near the crystalline-amorphous interface may also benefit the fast recrystallization of GST-SL.

4. Conclusion

In summary, this work uncovers the long-term puzzle of melting behaviors in GST-SL using a large-scale MLIP MD simulation for the first time. Compared to traditional RS-GST, GST-SL is easier to maintain its crystalline phase under an overheated condition owing to the stable vdW interfaces. The melting of GST-SL is initiated by the formation of the unique CiV defects while the melting of RS-GST can be activated by the pre-existed vacancies. In other words, both the melting processes in GST-SL and RS-GST are nucleated via structural defects. The formation of the CiV defect requires chain-like movement of atoms and vacancy-assisted site exchange to form an anti-site defect, so it takes a relatively long time to occur. More importantly, the melting of GST-SL is completed via the *sparse nucleation and growth* of the defect-initiated liquid regions. In contrast, the melting of RS-GST simultaneously takes place at anywhere of the lattice due to a large amount of randomly distributed intrinsic vacancies which act as ultra-dense seeds of nuclei. As a result of the different melting mechanisms, the melting regions in GST-SL can be spatially localized and readily controlled, suggesting a strong possibility of partial melting, while the melting of RS-GST occurs homogenously and very quickly throughout the lattice. In addition, the atomic distribution after melting in GST-SL, at least near the nano crystalline-liquid interface, is more chemically ordered than that in RS-GST. The present results not only uncover the special melting behavior in GST-SL but also provide critical references to understand the reason behind the low power consumption in GST-SL PCM devices. The present study will provide an important theoretical basis for the development of advanced PCM applications based on superlattice materials.

CRediT authorship contribution statement

Bai-Qian Wang: Data curation, Formal analysis, Investigation, Validation, Visualization, Writing – original draft. **Tian-Yu Zhao:** Data curation, Formal analysis, Validation. **Huan-Ran Ding:** Data curation, Validation. **Yu-Ting Liu:** Formal analysis, Validation. **Nian-Ke Chen:** Conceptualization, Methodology, Supervision, Writing – review & editing. **Meng Niu:** Data curation, Validation. **Xiao-Dong Li:** Validation. **Ming Xu:** Methodology, Writing – review & editing. **Hong-Bo Sun:** Resources, Supervision, Writing – review & editing. **Shengbai Zhang:** Data curation, Supervision, Validation, Writing – review & editing. **Xian-Bin Li:** Conceptualization, Data curation, Funding acquisition, Investigation, Project administration, Supervision, Writing – review & editing.

Declaration of competing interest

The authors declare that they have no known competing financial interests or personal relationships that could have appeared to influence the work reported in this paper.

Acknowledgment

This work was supported by the National Science and Technology Major Project (Grant No. 2022ZD0117600), the National Natural Science Foundation of China (Grants No. 12274172 and 12274180), and the Natural Science Foundation of Jilin Province (20230101007JC). High-Performance Computing Center (HPCC) at Jilin University is also acknowledged.

Supplementary materials

Supplementary material associated with this article can be found, in the online version, at doi:10.1016/j.actamat.2024.120123.

References

[1] S.W. Fong, C.M. Neumann, H.S.P. Wong, Phase-change memory—Towards a storage-class memory, IEEE Trans. Electron Devices 64 (2017) 4374–4385.
[2] T. Kim, S. Lee, Evolution of phase-change memory for the storage-class memory and beyond, IEEE Trans. Electron Devices 67 (2020) 1394–1406.
[3] G.W. Burr, R.M. Shelby, A. Sebastian, S. Kim, S. Kim, S. Sidler, K. Virwani, M. Ishii, P. Narayanan, A. Fumarola, L.L. Sanches, I. Boybat, M.Le Gallo, K. Moon, J. Woo, H. Hwang, Y. Leblebici, Neuromorphic computing using non-volatile memory, Adv. Phys.: X 2 (2017) 89–124.
[4] A.I. Khan, H. Yu, H. Zhang, J.R. Goggin, H. Kwon, X. Wu, C. Perez, K.M. Neilson, M. Asheghi, K.E. Goodson, P.M. Vora, A. Davydov, I. Takeuchi, E. Pop, Energy efficient neuro-inspired phase–change memory based on $Ge_4Sb_6Te_7$ as a novel epitaxial nanocomposite, Adv. Mater. 35 (2023) 2300107.
[5] D. Ielmini, H.S.P. Wong, In-memory computing with resistive switching devices, Nat. Electron. 1 (2018) 333–343.
[6] M.Le Gallo, A. Sebastian, R. Mathis, M. Manica, H. Giefers, T. Tuma, C. Bekas, A. Curioni, E. Eleftheriou, Mixed-precision in-memory computing, Nat. Electron. 1 (2018) 246–253.
[7] A. Sebastian, M.Le Gallo, R. Khaddam-Aljameh, E. Eleftheriou, Memory devices and applications for in-memory computing, Nat. Nanotechnol. 15 (2020) 529–544.
[8] P. Hosseini, C.D. Wright, H. Bhaskaran, An optoelectronic framework enabled by low-dimensional phase-change films, Nature 511 (2014) 206–211.
[9] D.J. Broer, A new view on displays, Nature 511 (2014) 159–160.
[10] C. Ríos, M. Stegmaier, P. Hosseini, D. Wang, T. Scherer, C.D. Wright, H. Bhaskaran, W.H.P. Pernice, Integrated all-photonic non-volatile multi-level memory, Nat. Photonics. 9 (2015) 725–732.
[11] Y.F. Zhang, C. Fowler, J.H. Liang, B. Azhar, M.Y. Shalaginov, S. Deckoff-Jones, S. S. An, J.F.B. Chou, C.M. Roberts, V. Liberman, M.K. Kang, C. Rios, K.A. Richardson, C. Rivero-Baleine, T. Gu, H.L. Zhang, J.J. Hu, Electrically reconfigurable non-volatile metasurface using low-loss optical phase-change material, Nat. Nanotechnol. 16 (2021) 661–666.
[12] W. Zhou, B. Dong, N. Farmakidis, X. Li, N. Youngblood, K. Huang, Y. He, C. David Wright, W.H.P. Pernice, H. Bhaskaran, In-memory photonic dot-product engine with electrically programmable weight banks, Nat. Commun. 14 (2023) 2887.
[13] B.Q. Wang, X.B. Li, H.B. Sun, In-memory computing based on photonic-electronic hybrid phase-change cells, Sci. Bull. 68 (2023) 2500–2502.
[14] J.J. Yang, D.B. Strukov, D.R. Stewart, Memristive devices for computing, Nat. Nanotechnol. 8 (2013) 13–24.
[15] F. Xiong, A.D. Liao, D. Estrada, E. Pop, Low-power switching of phase-change materials with carbon nanotube electrodes, Science 332 (2011) 568–570.
[16] W.I. Park, B.K. You, B.H. Mun, H.K. Seo, J.Y. Lee, S. Hosaka, Y. Yin, C.A. Ross, K. J. Lee, Y.S. Jung, Self-assembled incorporation of modulated block copolymer nanostructures in phase-change memory for switching power reduction, ACS Nano 7 (2013) 2651–2658.
[17] C. Ahn, S.W. Fong, Y. Kim, S. Lee, A. Sood, C.M. Neumann, M. Asheghi, K. E. Goodson, E. Pop, H.S.P. Wong, Energy-efficient phase-change memory with graphene as a thermal barrier, Nano Lett 15 (2015) 6809–6814.

[18] Y.T. Liu, X.B. Li, H. Zheng, N.K. Chen, X.P. Wang, X.L. Zhang, H.B. Sun, S. Zhang, High-throughput screening for phase-change memory materials, Adv. Funct. Mater. 31 (2021) 2009803.

[19] N.K. Chen, X.B. Li, X.P. Wang, M.J. Xia, S.Y. Xie, H.Y. Wang, Z. Song, S. Zhang, H. B. Sun, Origin of high thermal stability of amorphous $Ge_1Cu_2Te_3$ alloy: A significant Cu-bonding reconfiguration modulated by Te lone-pair electrons for crystallization, Acta Mater 90 (2015) 88–93.

[20] F. Rao, K. Ding, Y. Zhou, Y. Zheng, M. Xia, S. Lv, Z. Song, S. Feng, I. Ronneberger, R. Mazzarello, W. Zhang, E. Ma, Reducing the stochasticity of crystal nucleation to enable subnanosecond memory writing, Science 358 (2017) 1423–1427.

[21] M. Zhu, M. Xia, F. Rao, X. Li, L. Wu, X. Ji, S. Lv, Z. Song, S. Feng, H. Sun, S. Zhang, One order of magnitude faster phase change at reduced power in Ti-Sb-Te, Nat. Commun. 5 (2014) 4086.

[22] R.E. Simpson, P. Fons, A.V. Kolobov, T. Fukaya, M. Krbal, T. Yagi, J. Tominaga, Interfacial phase-change memory, Nat. Nanotechnol. 6 (2011) 501–505.

[23] J. Hegedüs, S.R. Elliott, Microscopic origin of the fast crystallization ability of Ge–Sb–Te phase-change memory materials, Nat. Mater. 7 (2008) 399–405.

[24] A.V. Kolobov, P. Fons, A.I. Frenkel, A.L. Ankudinov, J. Tominaga, T. Uruga, Understanding the phase-change mechanism of rewritable optical media, Nat. Mater. 3 (2004) 703–708.

[25] S. Raoux, F. Xiong, M. Wuttig, E. Pop, Phase change materials and phase change memory, MRS Bull 39 (2014) 703–710.

[26] J. Zhao, A.I. Khan, M.Y. Efremov, Z. Ye, X. Wu, K. Kim, Z. Lee, H.S.P. Wong, E. Pop, L.H. Allen, Probing the melting transitions in phase-change superlattices via thin film nanocalorimetry, Nano Lett 23 (2023) 4587–4594.

[27] N. Takaura, T. Ohyanagi, M. Tai, M. Kinoshita, K. Akita, T. Morikawa, H. Shirakawa, M. Araidai, K. Shiraishi, Y. Saito, J. Tominaga, 55-μA Ge_xTe_{1-x}/Sb_2Te_3 superlattice topological-switching random access memory (TRAM) and study of atomic arrangement in Ge-Te and Sb-Te structures, in: 2014 IEEE International Electron Devices Meeting, 2014, 29.2.1-29.2.4.

[28] J. Momand, R. Wang, J.E. Boschker, M.A. Verheijen, R. Calarco, B.J. Kooi, Interface formation of two- and three-dimensionally bonded materials in the case of GeTe–Sb_2Te_3 superlattices, Nanoscale 7 (2015) 19136–19143.

[29] T. Ohyanagi, M. Kitamura, M. Araidai, S. Kato, N. Takaura, K. Shiraishi, GeTe sequences in superlattice phase change memories and their electrical characteristics, Appl. Phys. Lett. 104 (2014) 252106.

[30] J. Tominaga, A.V. Kolobov, P. Fons, T. Nakano, S. Murakami, Ferroelectric order control of the dirac-semimetal phase in GeTe-Sb_2Te_3 superlattices, Adv. Mater. Interfaces. 1 (2014) 1300027.

[31] X. Yu, J. Robertson, Atomic layering, intermixing and switching mechanism in Ge-Sb-Te based chalcogenide superlattices, Sci. Rep. 6 (2016) 37325.

[32] Y.S. Song, J. Kim, S.H. Jhi, Pair potential modeling of atomic rearrangement in GeTe-Sb_2Te_3 superlattice via first-principles calculations, J. Appl. Phys. 121 (2017) 095102.

[33] H. Nakamura, I. Rungger, S. Sanvito, N. Inoue, J. Tominaga, Y. Asai, Resistive switching mechanism of GeTe–Sb_2Te_3 interfacial phase change memory and topological properties of embedded two-dimensional states, Nanoscale 9 (2017) 9386–9395.

[34] N.K. Chen, X.B. Li, X.P. Wang, S.Y. Xie, W.Q. Tian, S. Zhang, H.B. Sun, Metal–insulator transition of Ge–Sb–Te superlattice: An electron counting model study, IEEE Trans. Nanotechnol. 17 (2018) 140–146.

[35] J. Kalikka, X. Zhou, E. Dilcher, S. Wall, J. Li, R.E. Simpson, Strain-engineered diffusive atomic switching in two-dimensional crystals, Nat. Commun. 7 (2016) 11983.

[36] X. Zhou, J. Kalikka, X. Ji, L. Wu, Z. Song, R.E. Simpson, Phase-change memory materials by design: a strain engineering approach, Adv. Mater. 28 (2016) 3007–3016.

[37] A.I. Khan, H. Kwon, M.E. Chen, M. Asheghi, H.S.P. Wong, K.E. Goodson, E. Pop, Electro-thermal confinement enables improved superlattice phase change memory, IEEE Electron Device Lett 43 (2022) 204–207.

[38] X.B. Li, N.K. Chen, X.P. Wang, H.B. Sun, Phase-change superlattice materials toward low power consumption and high density data storage: Microscopic picture, working principles, and optimization, Adv. Funct. Mater. 28 (2018) 1803380.

[39] Y. Hu, H. Zou, J. Zhang, J. Xue, Y. Sui, W. Wu, L. Yuan, X. Zhu, S. Song, Z. Song, $Ge_2Sb_2Te_5$/Sb superlattice-like thin film for high speed phase change memory application, Appl. Phys. Lett. 107 (2015) 263105.

[40] J. Shen, S. Lv, X. Chen, T. Li, S. Zhang, Z. Song, M. Zhu, Thermal barrier phase change memory, ACS Appl. Mater. Interfaces 11 (2019) 5336–5343.

[41] V. Evang, R. Mazzarello, Absence of Partial Amorphization in GeSbTe Chalcogenide Superlattices, Phys. Status Solidi - Rapid Res. Lett. 15 (2020).

[42] M. Boniardi, J.E. Boschker, J. Momand, B.J. Kooi, A. Redaelli, R. Calarco, Evidence for Thermal-Based Transition in Super-Lattice Phase Change Memory, Phys. Status Solidi - Rapid Res. Lett. 13 (2019).

[43] H. Kwon, A.I. Khan, C. Perez, M. Asheghi, E. Pop, K.E. Goodson, Uncovering thermal and electrical properties of Sb_2Te_3/GeTe superlattice films, Nano Lett 21 (2021) 5984–5990.

[44] A.P. Bartok, M.C. Payne, R. Kondor, G. Csanyi, Gaussian approximation potentials: The accuracy of quantum mechanics, without the electrons, Phys. Rev. Lett. 104 (2010) 136403.

[45] J. Behler, Neural network potential-energy surfaces in chemistry: a tool for large-scale simulations, Phys. Chem. Chem. Phys. 13 (2011) 17930–17955.

[46] Z. Deng, C. Chen, X.G. Li, S.P. Ong, An electrostatic spectral neighbor analysis potential for lithium nitride, NPJ Comput. Mater. 5 (2019) 75.

[47] K. Gubaev, E.V. Podryabinkin, G.L.W. Hart, A.V. Shapeev, Accelerating high-throughput searches for new alloys with active learning of interatomic potentials, Comput. Mater. Sci. 156 (2019) 148–156.

[48] G.C. Sosso, J. Behler, M. Bernasconi, Breakdown of Stokes–Einstein relation in the supercooled liquid state of phase change materials, Phys. Status Solidi (B): Basic Res. 249 (2012) 1880–1885.

[49] G.C. Sosso, J. Colombo, J. Behler, E. Del Gado, M. Bernasconi, Dynamical heterogeneity in the supercooled liquid state of the phase change material GeTe, J. Phys. Chem. B 118 (2014) 13621–13628.

[50] G.C. Sosso, M. Salvalaglio, J. Behler, M. Bernasconi, M. Parrinello, Heterogeneous crystallization of the phase change material GeTe via atomistic simulations, J. Phys. Chem. C 119 (2015) 6428–6434.

[51] F.C. Mocanu, K. Konstantinou, T.H. Lee, N. Bernstein, V.L. Deringer, G. Csányi, S. R. Elliott, Modeling the phase-change memory material, $Ge_2Sb_2Te_5$, with a machine-learned interatomic potential, J. Phys. Chem. B 122 (2018) 8998–9006.

[52] K. Konstantinou, F.C. Mocanu, T.-H. Lee, S.R. Elliott, Revealing the intrinsic nature of the mid-gap defects in amorphous Ge2Sb2Te5, Nat. Commun. 10 (2019) 3065.

[53] F.C. Mocanu, K. Konstantinou, S.R. Elliott, Quench-rate and size-dependent behaviour in glassy Ge2Sb2Te5 models simulated with a machine-learned Gaussian approximation potential, J. Phys. D: Appl. Phys 53 (2020) 244002.

[54] P. Rajak, K. Liu, A. Krishnamoorthy, R.K. Kalia, A. Nakano, K.i. Nomura, S. C. Tiwari, P. Vashishta, Neural network molecular dynamics at scale, in: 2020 IEEE International Parallel and Distributed Processing Symposium Workshops (IPDPSW), 2020, pp. 991–994.

[55] L. Yang, B.Y. Cao, Thermal transport of amorphous phase change memory materials using population-coherence theory: A first-principles study, J. Phys. D: Appl. Phys. 54 (2021) 505302.

[56] Y. Zhou, W. Zhang, E. Ma, V.L. Deringer, Device-scale atomistic modelling of phase-change memory materials, Nat. Electron. 6 (2023) 746–754.

[57] Y.X. Zhou, H.Y. Zhang, V.L. Deringer, W. Zhang, Structure and dynamics of supercooled liquid $Ge_2Sb_2Te_5$ from machine-learning-driven simulations, Phys. Status Solidi - Rapid Res. Lett. 15 (2021) 2000403.

[58] A.P. Thompson, H.M. Aktulga, R. Berger, D.S. Bolintineanu, W.M. Brown, P. S. Crozier, P.J. in 't Veld, A. Kohlmeyer, S.G. Moore, T.D. Nguyen, R. Shan, M. J. Stevens, J. Tranchida, C. Trott, S.J. Plimpton, LAMMPS - A flexible simulation tool for particle-based materials modeling at the atomic, meso, and continuum scales, Comput. Phys. Commun. 271 (2022) 108171.

[59] A.P. Bartók, R. Kondor, G. Csányi, On representing chemical environments, Phys. Rev. B 87 (2013) 184115.

[60] S. De, A.P. Bartok, G. Csanyi, M. Ceriotti, Comparing molecules and solids across structural and alchemical space, Phys. Chem. Chem. Phys. 18 (2016) 13754–13769.

[61] J.F. Justo, F. de Brito Mota, A. Fazzio, First-principles investigation of a SiN_x:H, Phys. Rev. B 65 (2002) 073202.

[62] J. Kalikka, J. Akola, R.O. Jones, Crystallization processes in the phase change material $Ge_2Sb_2Te_5$: Unbiased density functional/molecular dynamics simulations, Phys. Rev. B 94 (2016) 134105.

[63] S.W. Ryu, J.H. Oh, J.H. Lee, B.J. Choi, W. Kim, S.K. Hong, C.S. Hwang, H.J. Kim, Phase transformation behaviors of SiO_2 doped $Ge_2Sb_2Te_5$ films for application in phase change random access memory, Appl. Phys. Lett. 92 (2008) 142110.

[64] X. Yu, J. Robertson, Modeling of switching mechanism in GeSbTe chalcogenide superlattices, Sci. Rep. 5 (2015) 12612.

[65] Y. Xu, Y. Zhou, X.D. Wang, W. Zhang, E. Ma, V.L. Deringer, R. Mazzarello, Unraveling crystallization mechanisms and electronic structure of phase-change materials by large-scale ab initio simulations, Adv. Mater. 34 (2022) e2109139.

[66] V.L. Deringer, N. Bernstein, G. Csanyi, C. Ben Mahmoud, M. Ceriotti, M. Wilson, D. A. Drabold, S.R. Elliott, Origins of structural and electronic transitions in disordered silicon, Nature 589 (2021) 59–64.

[67] J. Mavracic, F.C. Mocanu, V.L. Deringer, G. Csanyi, S.R. Elliott, Similarity between amorphous and crystalline phases: The case of TiO_2, J. Phys. Chem. Lett. 9 (2018) 2985–2990.